

Image-Based Reconstruction for a 3D-PFHS Heat Transfer Problem by ReConNN

Yu Li^{a, *}, Hu Wang^{a, **}, Xinjian Deng^a

a. State Key Laboratory of Advanced Design and Manufacturing for Vehicle Body, Hunan University, Changsha, 410082, PR China

Highlights

- i. The ReConNN model is suggested to reconstruct "from image-based model to analysis-based model" for 3D heat sink models.
- ii. A novel reconstruction method, 3D-2D-3D, for three-dimensional models is proposed.
- iii. The ReConNN is successfully applied to a heat transfer process of a PFHS.

Abstract

The heat transfer performance of Plate Fin Heat Sink (PFHS) has been investigated experimentally and extensively. Commonly, the objective function of PFHS design is based on the responses of simulations. Compared with existing studies, the purpose of this work is to transfer from image-based model to analysis-based model for heat sink designs. It means that the sequential optimization should be based on images instead of responses. Therefore, an image-based reconstruction model of a heat transfer process for a 3D-PFHS is established. Unlike image recognition, such procedure cannot be implemented by existing recognition algorithms (e.g. Convolutional Neural Network) directly. Therefore, a Reconstructive Neural Network (ReConNN), integrated supervised learning and unsupervised learning techniques, is suggested. According to the experimental results, the heat transfer process can be observed more detailed and clearly, and the reconstructed results are meaningful for the further optimizations.

* First author. *E-mail address:* liyuhnu@hnu.edu.cn (Y. Li)

** Corresponding author. Tel.: +86 0731 88655012; fax: +86 0731 88822051.

E-mail address: wanghu@hnu.edu.cn (H. Wang)

Nomenclature

t_w	temperature of wall	$p(y/\mathbf{x})$	softmax output of label
t_f	temperature of fluid	$p(y)$	overall labels distribution
n	exterior normal of wall		
h	coefficient of heat transfer	<i>Greek symbols</i>	
c	specific heat capacity	τ	time
$\dot{\Phi}$	internal heat source	λ	thermal conductivity
u	velocity component along x -axis	ρ	density
v	velocity component along y -axis	Δ	Laplace operator
w	velocity component along z -axis	η	kinetic viscosity
F_x	body force along x -axis	λ	thermal conductivity
F_y	body force along y -axis	θ	initial parameter
F_z	body force along z -axis	ρ_1	attenuation coefficient
p	pressure	ρ_2	attenuation coefficient
c_p	specific heat at constant pressure	ε	learning rate
$L(x)$	loss function	μ	random value between 0 and 1
x_i	training sample		
s	first moment estimation	<i>Subscripts</i>	
r	second moment estimation	w	wall
y_i	actual value	f	fluid
\hat{y}_i	predicted value	x	x -axis
STD	standard deviation	y	y -axis
MSE	mean square error	z	z -axis
\mathbf{x}	sample set	p	pressure

1. Introduction

Over recent years, the electronics industry is increasingly prosperous, and increasing the heat transfer efficiency of electronic components has become an important topic of research and development. Wang [1] presented flow visualization and frictional results of enlarged fin-and-tube heat exchangers with and without the presence of vortex generators. He found that the delta winglet caused more intensely vortical motion and flow unsteadiness than the annular winglet. Ahmed [2] gave an overview about the early studies done in order to improve the performance of thermal systems. Additionally, he also summarized the recent experimental and numerical developments on the Numerical Heat Transfer (NHT). Huisseune [3] numerically

investigated the effect of punching delta winglet vortex generators into the louvered fin surface near the wake region of each tube. Additionally, he [4] studied the influence of the louver and delta winglet geometry on the thermal and hydraulic performance of a compound heat exchanger. Sinha [5] performed numerical investigations pertaining to heat transfer enhancement of a plate-fin heat exchanger by using two rows of winglet type Vortex Generators (VG). Chiang [6] applied Taguchi method to predict and optimize the cooling performance of Parallel-Plain Fin (PPF) heat sink. In his study, the optimum design parameters of the lowest value of the highest temperature were found. Chingulpitak [7] summarized the publications with respect to research on the fluid flow directions and behaviors through heat sinks which offered guidelines for future researches. Chen [8] proposed a novel air-cooled heat sink profile termed as Interleaved Parallelogram Fin Module (IPFM). The IPFM not only gained the advantage of lower pressure drop, but also obtained a material saving. Moreover, he [9] studied a quick weight saving methodology with trapezoidal base heat sink applicable for electronic cooling application. Damook [10] investigated the benefits of using pin fin heat sinks with multiple perforations. In addition, an experimental heat sink with multiple perforations was also designed.

As air flows over a network of fins, convective heat transfer is the most common technique to cool electronics for low cost, availability and reliability [11]. The surface fins are able to achieve large heat transfer area and act as turbulence promoters for a further enhance of heat transfer rate, without excessive primary surface area. PFHSs are commonly used due to their simple structure and ease of manufacturing. Many works about PFHSs have been studied, e.g. Joo [12] compared the thermal performance of optimized plate-fin and pin-fin heat sinks with a vertically oriented base plate, and proposed a new correlation of the heat transfer coefficient. Because of the many design parameters and the critical issue of developing both cost and thermal effective, Ventola [13] presented a novel thermal model of PFHS. Hossain [14] developed an analytical model to predict air flow and pressure drop. The model applied conservation of mass and momentum over the bypass regions and established flow channels between fins. Li [15] assessed the performance of PFHSs in a cross

flow. Experimental results indicated that increasing the Reynolds number could reduce the thermal resistance of the heat sink. Subsequently, he [16] investigated the thermal-fluid characteristics of a flat-fin heat sink with a pair of vortex generators. Srisomporn [17] demonstrated the practical multiobjective optimization of PFHSs and pointed out the superiority of using a combined response surface method and multiobjective evolutionary optimizer. Zhou [18] proposed a multiparameter constrained optimization procedure to design the PFHSs by minimizing their rates of entropy generation and three cases demonstrated the feasibility of the algorithm. Rao [19] presented the multiobjective design optimization of a PFHS equipped with flow-through and impingement-flow air cooling systems. Chen [20] developed a multiobjective real-coded genetic algorithm for the optimal heat sink design problem. Chen [21] applied the inverse method in conjunction with the experimental temperature data to investigate the accuracy of the heat transfer coefficient on the fin in the PFHS. Kim [22] optimized thermal performance of a vertical PFHS under natural convection.

Neural Network (NN) is applied in this study to construct surrogate models for a three-dimensional PFHS to refine the heat transfer process and for further optimizations. This NN-based reconstruction transfers from image-based model to analysis-based model. In other words, the structural optimizations should be based on images instead of responses. To complete this study, Reconstructive Neural Network (ReConNN) proposed by Li [23] is employed. It is well known that some Machine Learning (ML) methods, including the ANN which is the core technology of Deep Learning (DL), have been utilized in NHT, such as Shiguemori [24] described a methodology for using NNs in an inverse heat conduction problem to determine the initial temperature profile on a slab with adiabatic boundary condition. Sablani [25] accomplished the Inverse Heat Conduction Problem (IHCP) dealing with the estimation of the heat transfer coefficient for a solid/fluid by using a NN. Baby [26] determined the time to reach a set-point temperature for aluminum finned heat sinks filled with the phase change material n-eicosane. Then he integrated the results with a NN to predict operating times. Cz d [27] proposed a NN-based solution of the inverse

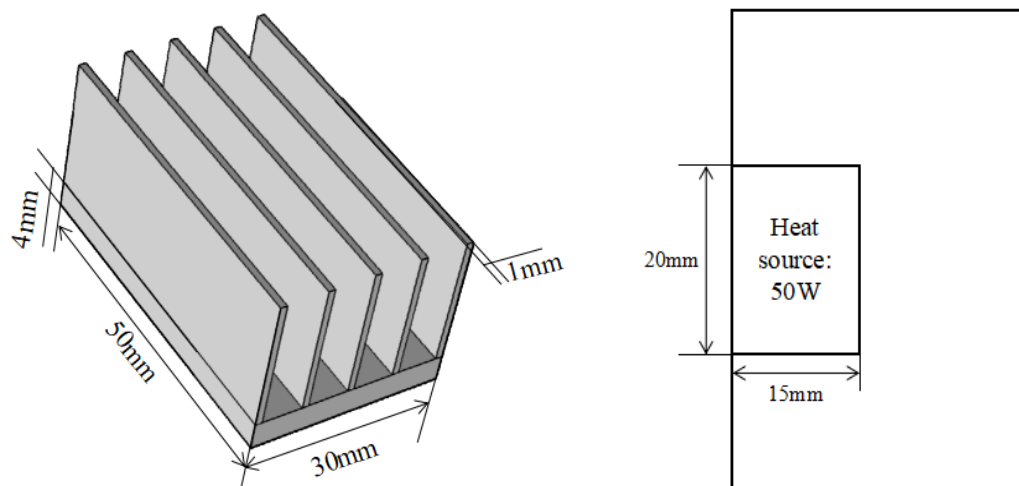
heat conduction problem of identifying the temperature-dependent volumetric heat capacity function of a solid material. Razavi [28] used NN to model the thermal performance of an underground cold-water cistern. Aminian [29] applied NNs to predict the thermal conductivity of nanofluids. Colorado [30] employed NNs to design a physical–empirical model to describe heat transfer of helical coil in oil and glycerol/water solution.

In this study, in order to refine the heat transfer process and to obtain a better optimization process, a novel reconstruction method, 3D-2D-3D, for three-dimensional models is designed by using NNs. The slicing helps us to achieve the process of 3D-2D-3D simply. Moreover, unsupervised learning technique is employed to refine the transfer process, and supervised learning method is utilized to realize the image-based optimization. Lagrange interpolation algorithm completes the reconstruction. Ultimately, the reconstruction of a heat transfer process of a PFHS is studied to validate the effectiveness reconstruction method.

2. PFHS descriptions

2.1. Physical model

The 3D-steady-state CAD model of the PFHS is presented in Fig. 1, and its geometric parameters and boundary conditions are also marked. The heat sink is made of aluminum alloy material. Furthermore, effects of gravity and radiative heat transfer are neglected.



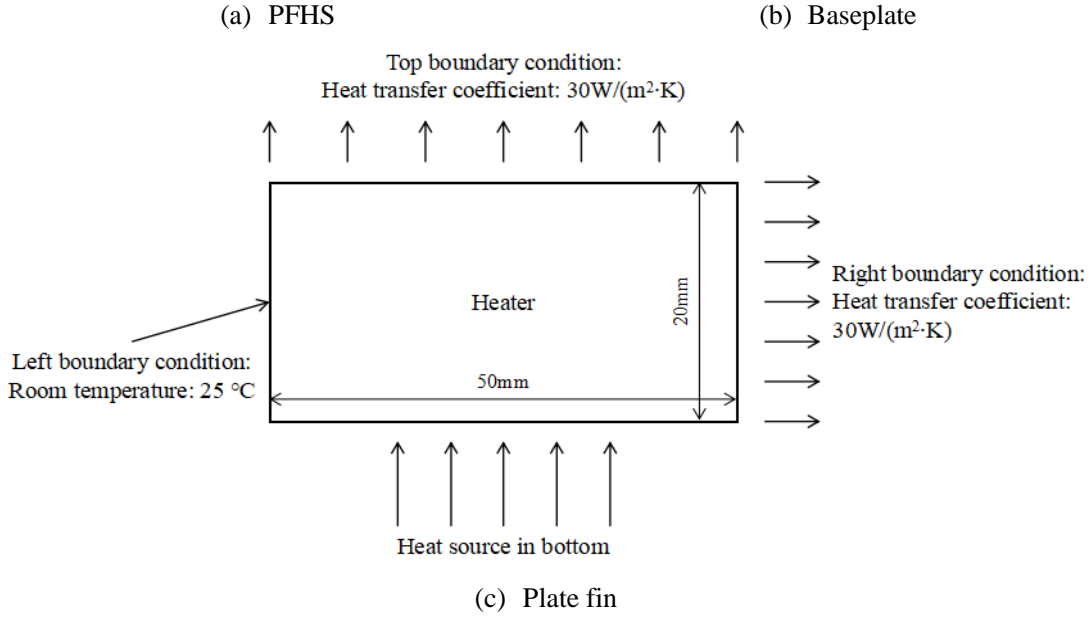


Fig. 1. CAD model of the PFHS.

2.2. Mathematical model

As shown in Fig. 1, the left of the PFHS is a Dirichlet Problem, it can be expressed as

$$t_w = f(\tau) \quad (1)$$

The top and right sides of the PFHS are Robin Problems, which are represented as

$$-\lambda \left(\frac{\partial t}{\partial n} \right)_w = h(t_w - t_f) \quad (2)$$

where τ is time; t_w and t_f are the temperatures of the wall and fluid, respectively; n is the exterior normal of the wall; h is the coefficient of heat transfer; and λ is the thermal conductivity.

The differential equation of a three-dimensional heat conduction in Cartesian coordinates is

$$\rho c \frac{\partial t}{\partial \tau} = \frac{\partial}{\partial x} \left(\lambda \frac{\partial t}{\partial x} \right) + \frac{\partial}{\partial y} \left(\lambda \frac{\partial t}{\partial y} \right) + \frac{\partial}{\partial z} \left(\lambda \frac{\partial t}{\partial z} \right) + \dot{\Phi} \quad (3)$$

Considering it is a steady state and constant property problem with internal heat source in this study, the differential equation can be simplified as Poisson equation:

$$\frac{\partial^2 t}{\partial x^2} + \frac{\partial^2 t}{\partial y^2} + \frac{\partial^2 t}{\partial z^2} + \frac{\dot{\Phi}}{\lambda} = 0 \quad (4)$$

that

$$\Delta t + \frac{\dot{\Phi}}{\lambda} = 0 \quad (5)$$

where ρ is density; c is specific heat capacity; $\dot{\Phi}$ is internal heat source; and Δ is Laplace operator.

Governing equation can be expressed as follows.

Mass conservation equation:

$$\frac{\partial u}{\partial x} + \frac{\partial v}{\partial y} + \frac{\partial w}{\partial z} = 0 \quad (6)$$

where u , v and w are velocity components of fluid along x -axis, y -axis and z -axis, respectively.

Momentum conservation equation:

$$\begin{cases} \rho \left(\frac{\partial u}{\partial \tau} + u \frac{\partial u}{\partial x} + v \frac{\partial u}{\partial y} + w \frac{\partial u}{\partial z} \right) = F_x - \frac{\partial p}{\partial x} + \eta \Delta u \\ \rho \left(\frac{\partial v}{\partial \tau} + u \frac{\partial v}{\partial x} + v \frac{\partial v}{\partial y} + w \frac{\partial v}{\partial z} \right) = F_y - \frac{\partial p}{\partial y} + \eta \Delta v \\ \rho \left(\frac{\partial w}{\partial \tau} + u \frac{\partial w}{\partial x} + v \frac{\partial w}{\partial y} + w \frac{\partial w}{\partial z} \right) = F_z - \frac{\partial p}{\partial z} + \eta \Delta w \end{cases} \quad (7)$$

where F_x , F_y and F_z are body forces along x -axis, y -axis and z -axis, respectively; p is pressure; η is kinetic viscosity

Energy conservation equation:

$$\rho c_p \left(\frac{\partial t}{\partial \tau} + u \frac{\partial t}{\partial x} + v \frac{\partial t}{\partial y} + w \frac{\partial t}{\partial z} \right) = \lambda \Delta t + \dot{\Phi} \quad (8)$$

where c_p is specific heat at constant pressure.

3. Image-based reconstruction of the heat transfer problem

In this study, the heat transfer process of the PFHS is reconstructed based on contour images. The reconstruction procedure is mainly composed of two issues,

image regression and image generation. To complete this task, ReConNN model is suggested.

The ReConNN is integrated of supervised learning and unsupervised learning algorithms. Firstly, the ReConNN is trained to map from contour images to objective functions by supervised learning method. Then, the unsupervised learning network is used to generate more reasonable contour images whose objective functions can be calculated by the trained supervised learning net. Finally, the simulation-based physical field can be reconstructed and refined according to Lagrange interpolation of the objective functions.

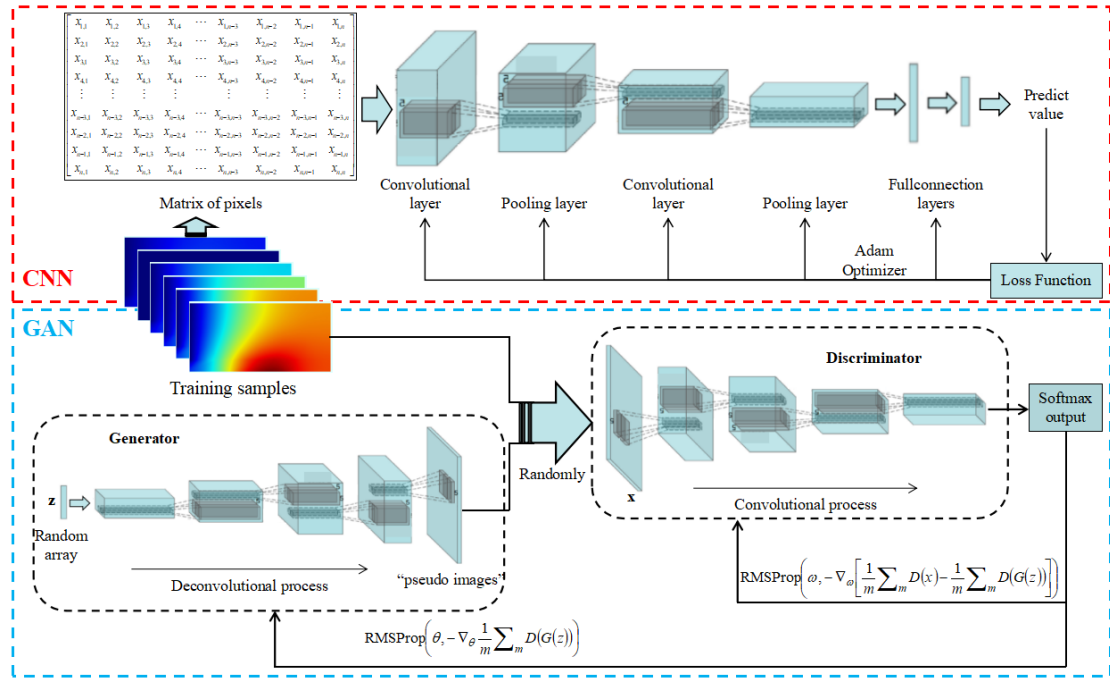


Fig. 2. Architecture of the ReConNN model.

As shown in Fig. 2, in the ReConNN, Convolutional Neural Network (CNN) [31] is used to construct the supervised learning model, and Generative Adversarial Network (GAN) [32] is applied to the unsupervised learning. In other words, the CNN constructs the mapping from contour images to objective functions laying the foundation for subsequent reconstruction and optimization, and the GAN generates "pseudo contour images" to reconstruct and refine the analysis-based model high-accurately.

Nevertheless, experiments in Section 4 of Ref. [23] showed that existing CNNs [33-35] might be difficult to handle image regression, and unsatisfied results were also achieved by existing GAN models [36-38] for mechanical problems. Therefore, a novel CNN architecture with image cutting, Convolution in Convolution (CIC), and an especial GAN model integrated with image compression, Compressed Wasserstein GAN (CWGAN)*, were introduced. As compared in Section 4.2 of Ref. [23], the CIC outperformed in terms of the number of samples trained per second, CPU percentage and accuracy criteria compared with other three popular CNN models. Simultaneously, the proposed CWGAN obtained the characteristics of the design images and helpful corresponding results also be achieved while other high performance GAN methods only generated images lacking convincing details and suffering blurred regions in most cases.

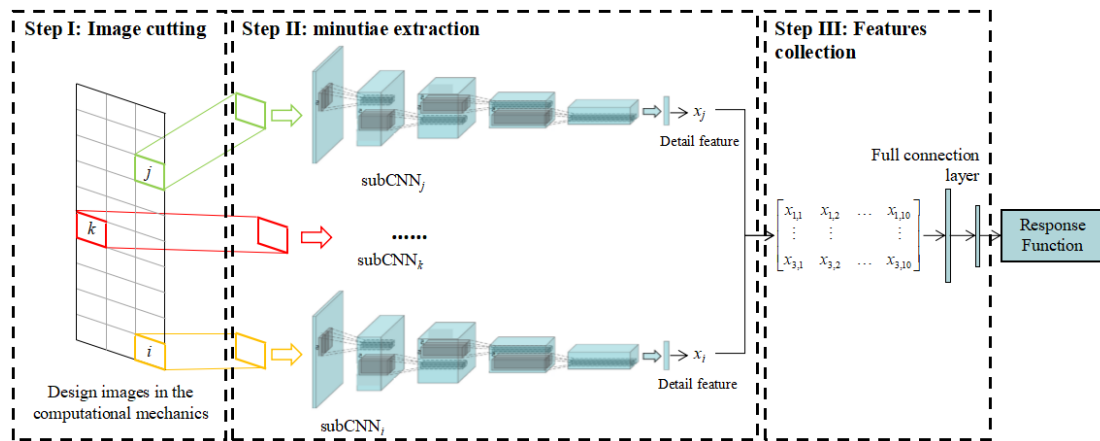


Fig. 3. Architecture of the CIC.

As shown in Fig. 3, the CIC can be mainly divided into three steps. In Step I, each image is divided to dozens of subimages by using image cutting technique. Subsequently, the detail features of each subimage are extracted through a separate subCNN. Ultimately, all features extracted in Step II are collected to obtain the response function in the final step. It is well known the details of simulation are important for designers for optimizations while popular CNNs might hardly obtain. Therefore, the aim of the CIC is to using separate sub-networks to improve the

* The name of the proposed GAN model has been updated as Compressed WGAN (CWGAN), which was CA-based WGAN (WGAN-CA).

extraction ability of detailed features.

The optimization algorithm utilized in the CIC is Adaptive Moment Estimation (Adam) optimizer which is essentially Root Mean Square Prop (RMSProp) with momentum factor. Adam integrates the advantages of AdaGrad and RMSProp, and spends lower computational cost. Furthermore, it performs well for most nonconvex optimization, large data sets, and high-dimensional space. Mathematically, the Adam can be defined as

$$g \leftarrow +\frac{1}{m} \nabla_{\theta} \sum_i L(f(x_i; \theta), y_i) \quad (9)$$

$$s \leftarrow \rho_1 s + (1 - \rho_1) g \quad (10)$$

$$r \leftarrow \rho_2 r + (1 - \rho_2) g \odot g \quad (11)$$

$$\hat{s} \leftarrow \frac{s}{1 - \rho_1} \quad (12)$$

$$\hat{r} \leftarrow \frac{r}{1 - \rho_2} \quad (13)$$

$$\Delta \theta = -\varepsilon \frac{\hat{s}}{\sqrt{\hat{r} + \delta}} \quad (14)$$

$$\theta \leftarrow \theta + \Delta \theta \quad (15)$$

where $L(x)$ is the loss function; θ is the initial parameter; x_i is a training sample; s and r are the first and second moment estimations, respectively; ρ_1 and ρ_2 are the attenuation coefficients; and ε is the learning rate. In this study, $\delta=10^{-8}$, $\rho_1=0.9$, and $\rho_2=0.999$.

For the CWGAN, in order to improve training accuracy and stability, image compression is introduced through a Convolutional Autoencoder (CA) [39], which is a classical convolutional encoder-decoder architecture. As shown in Fig. 4, the encoder contains three convolutional layers, followed by Leaky ReLU (LReLU) non-linearity and batchnorm-layer-based normalized. The decoder mirrors the encoder, and uses full connection layers to bring the output back to the distribution of the original input. Mathematically, the LReLU can be described as

$$\text{LReLU} = \max(x, \mu x) \quad (16)$$

where μ is a random value between 0 and 1. In this study, $\mu=0.2$.

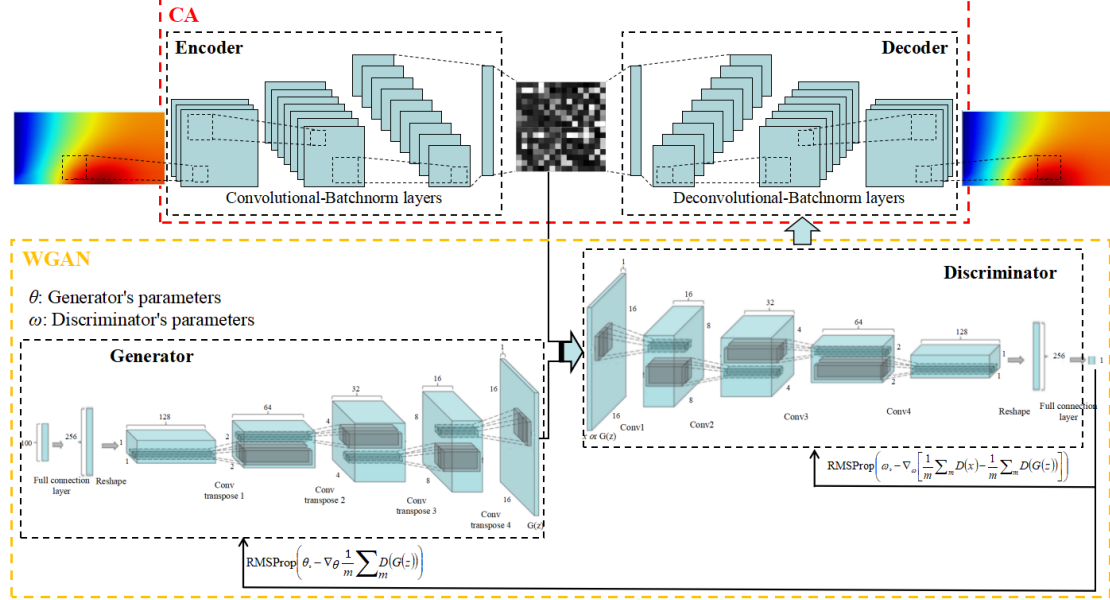


Fig. 4. Architecture of the CWGAN.

Batch normalization allows training to use much higher learning rates and be less careful about initialization [40]. For a layer with d -dimensional input $\mathbf{x}=(x_1, \dots, x_d)$, each dimension is normalized by batch normalization as

$$y_i = \gamma x_i^- + \beta \quad (17)$$

where

$$x_i^- = \frac{x_i - \mu_\beta}{\sigma_\beta} \quad (18)$$

s.t.

$$\mu_\beta = \frac{1}{d} \sum_{i=1}^d x_i \quad (19)$$

$$\sigma_\beta^2 = \frac{1}{d} \sum_{i=1}^d (x_i - \mu_\beta)^2 \quad (20)$$

where γ and β are parameters to be learned.

As shown in Fig. 4, the CA is trained to establish mappings both from contour images to $16 \times 16 \times 1$ gray level images and from $16 \times 16 \times 1$ gray level images to contour images. Through the CA, $16 \times 16 \times 1$ gray level images should be the new learning

distributions of the WGAN. Therefore, the WGAN-based NN is easier to be trained due to smaller input sizes.

To sum up, the detailed architecture of the ReConNN is shown in Table 1. The RMSProp optimization used in WGAN can be expressed as

$$g \leftarrow +\frac{1}{m} \nabla_{\theta} \sum_i L(f(x_i; \theta), y_i) \quad (21)$$

$$r \leftarrow \rho r + (1 - \rho) g \odot g \quad (22)$$

$$\Delta \theta = -\frac{\varepsilon}{\delta + \sqrt{r}} \odot g \quad (23)$$

$$\theta \leftarrow \theta + \Delta \theta \quad (24)$$

Table 1. Architecture of the ReConNN.

	No. of subimages	SubCNN architecture	Activation function	Optimization algorithm	
CIC	30	3 convolutional-mixed pooling	Leaky ReLU	Adam Optimizer	
	Subnet	Network architecture	Activation function	Optimization algorithm	
CWGAN	CA	Encoder	4 convolutional-batchnorm and 4 full connection	Leaky ReLU Adam	
		Decoder	4 full connection and 3 deconvolutional-batchnorm	Leaky ReLU Optimizer	
	WGAN	Generator	1 full connection and 2 deconvolutional-batchnorm	ReLU	RMSProp
		Discriminator	2 convolutional-batchnorm and 1 full connection	Leaky ReLU	Optimizer

4. Experiment results

In the previous sections, a three-dimensional CAD model of a PFHS and reconstruction method are suggested. In order to evaluate the performance of the reconstruction method for 3D PHHS, experiments and analyses are performed in this section.

4.1. PFHS samples

As shown in Fig. 5, considering the PFHS is three-dimensional and contains

five-plate fins and one baseplate, six cross sections, from A-A to F-F, are collected.

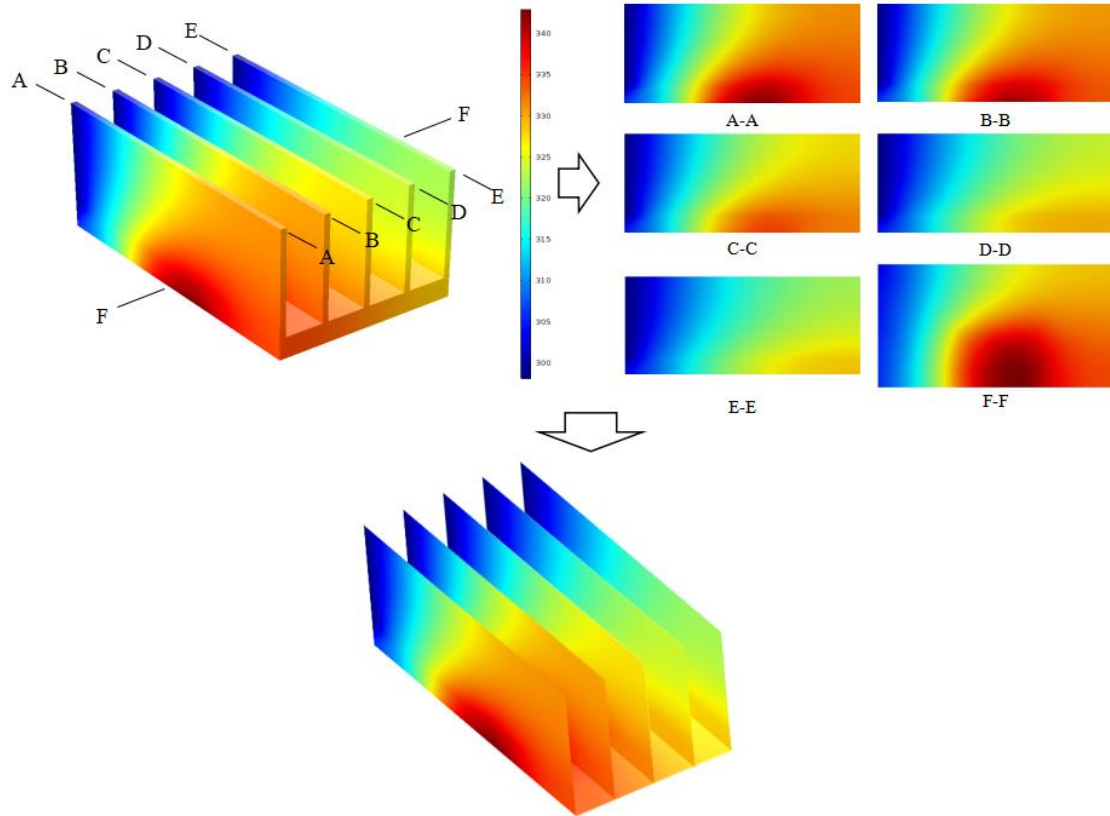


Fig. 5. The modeling process of 3D-2D-3D.

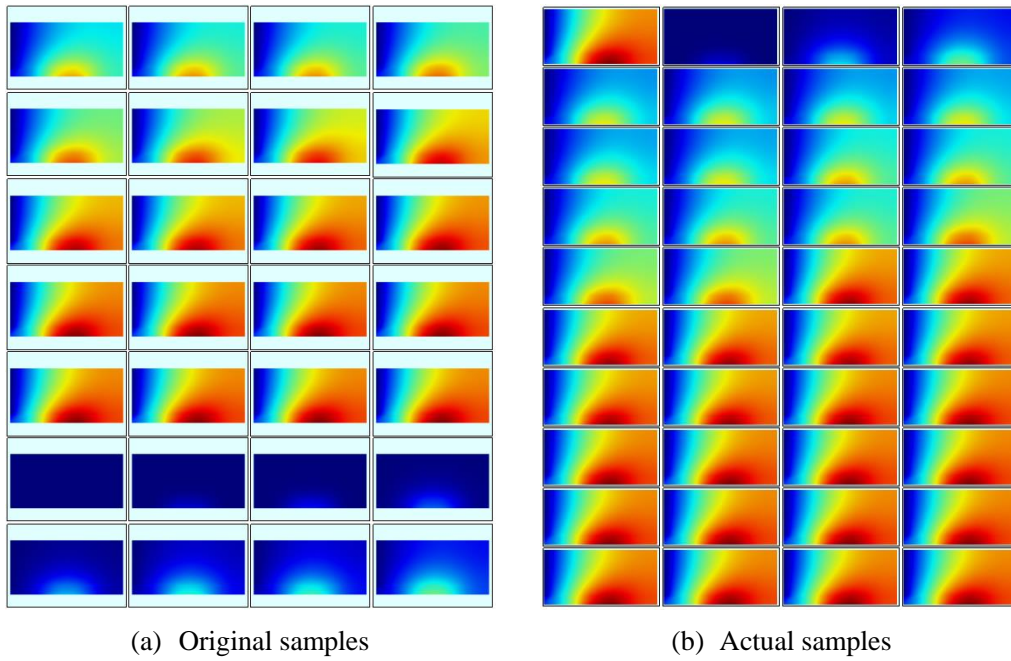


Fig. 6. Samples of five-plate fins.

The reconstruction of the PFHS can be divided into two issues. Firstly, because

of the same geometric parameters and environmental conditions, five-plate fins can be treated as one issue. In this study, 1,211 iterations run, and contour image in each iteration is collected as a training sample. Therefore, as shown in Fig. 6 (a), there are 6,055 ($=1,211 \times 5$) samples whose sizes are [886, 617, 3] for five-plate fins. However, the surrounding blank of each sample is useless, the actual sizes should be [850, 420, 3] as shown in Fig. 6 (b).

Another issue is the baseplate of the PFHS. As mentioned above, 1,211 iterations are run and 1,211 corresponding samples are collected. As shown in Fig. 7, original samples of the baseplate are [437, 308, 3]. Actually, [172, 282, 3] should be.

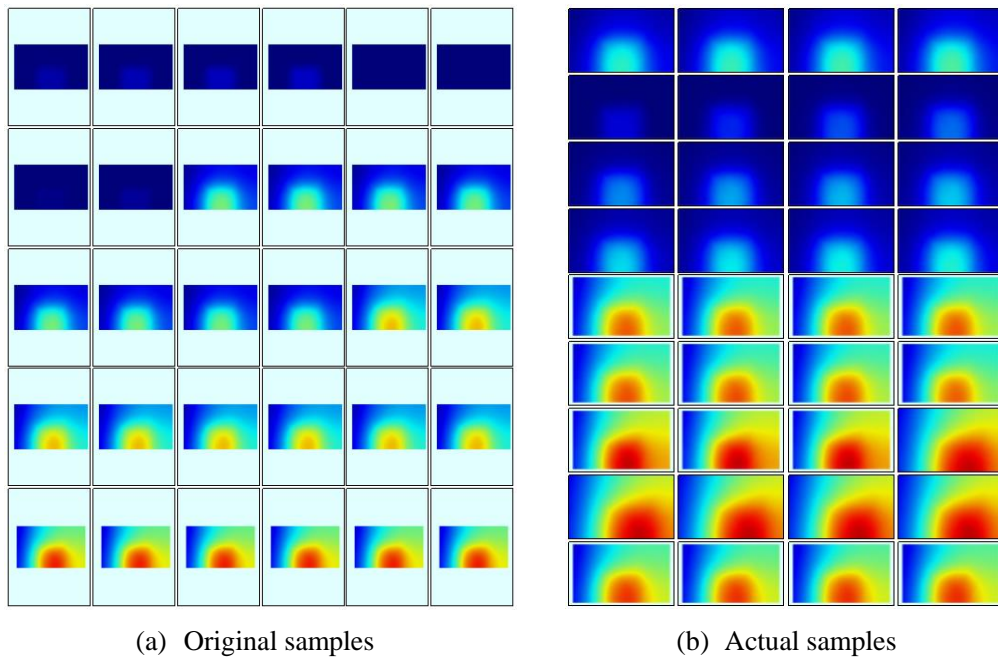


Fig. 7. Samples of the baseplate.

4.2. Training results of the CIC

In this section, three commonly used performance criteria [41], R Square (R^2), Relative Average Absolute Error (RAAE), and Relative Maximum Absolute Error (RMAE), as shown in Table 2, are employed for validating approximation models by the CIC. Moreover, in order to shown the relative error clearly, the following relative error (*Error*) is used to evaluate the accuracy of the CIC. Among them, y_i is the actual value, \hat{y}_i is the predicted value, STD stands for standard deviation, MSE (Mean Square Error) represents the departure of the metamodel from the real simulation

model, and the variance captures the irregular of the problem.

Table 2 Criteria for performance evaluation.

Criteria	Expression
RAAE	$\sum_{i=1}^n y_i - \hat{y}_i / (n \cdot \text{STD})$
RMAE	$\max(y_i - \hat{y}_i) / \text{STD}$
R^2	$1 - \frac{\sum_{i=1}^n (y_i - \hat{y}_i)^2}{\sum_{i=1}^n (y_i - \bar{y}_i)^2} = 1 - \frac{\text{MSE}}{\text{variance}}$
Error	$\frac{\ \hat{y} - y\ _2}{\ y\ _2} \times 100\%$

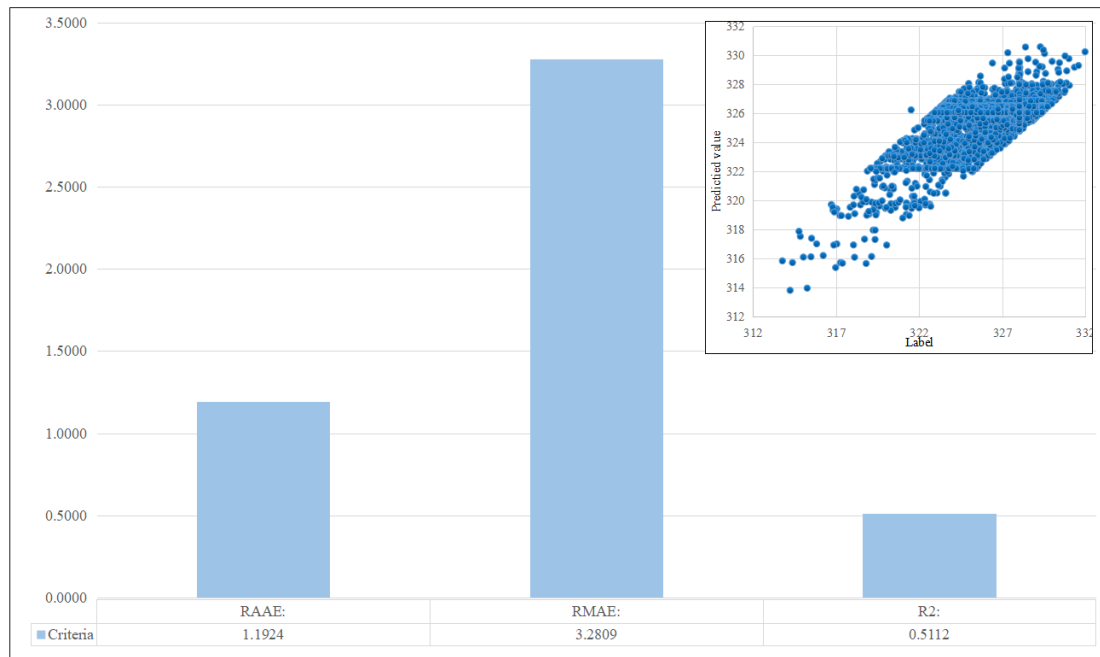


Fig. 7. Training results of the CIC for the five-plate fins.

Subsequently, samples are utilized to train the CIC for plate fins and baseplate. Training results are shown in Figs. 7 - 8. It can be found that R^2 for the two issues are more than 0.5, and RAAE and RMAE belong to 1 to 3. Considering the image regressions can be regarded as a thousands-dimensional modeling problem, the criteria are satisfied for the prediction. Moreover, according to the scatter diagram,

labels* and predicted values have a reasonable distribution. In addition, *Errors* correspondingly to the plate fins and baseplate are 0.5272% and 0.5527%, respectively. They further demonstrate the accuracy of the predicted objective functions.

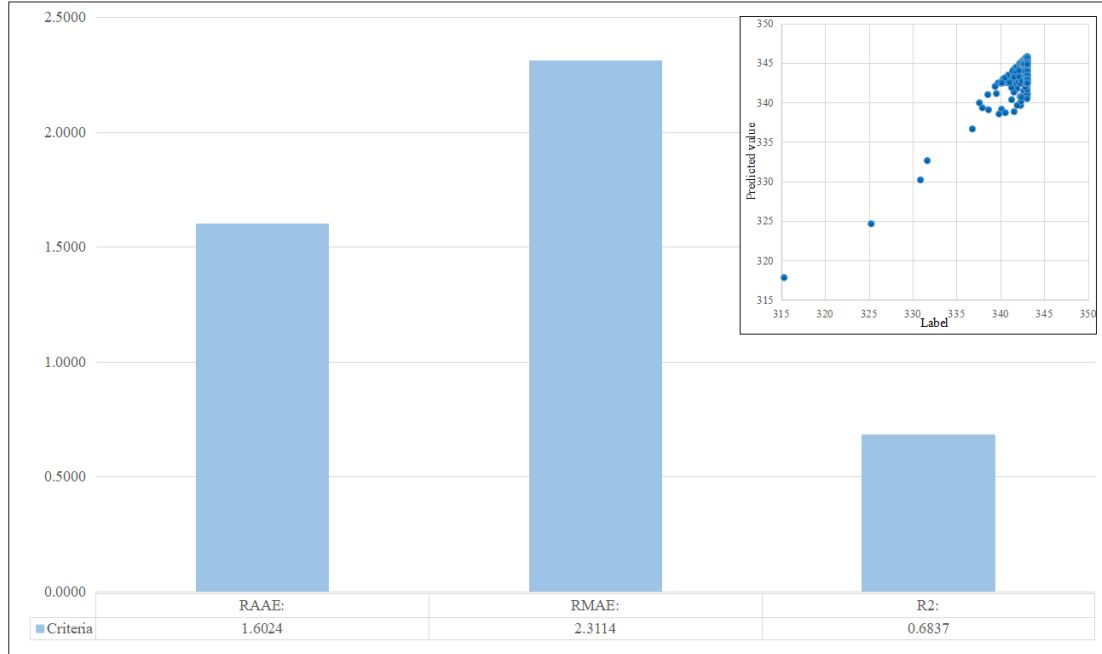


Fig. 8. Training results of the CIC for the baseplate.

4.3. Training results of the CWGAN

Firstly, the CA is trained. The training results are shown in Tables. 3 and 4. It can be seen that the CA constructs the relationship between contour images and $16 \times 16 \times 1$ gray level images commendably. Then the encoder of the trained CIC is used to compress the input samples to $16 \times 16 \times 1$ for WGAN.

Table 3. Training results of the CA for five-plate fins.








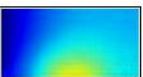
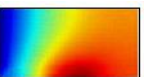


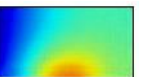

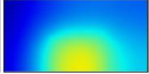
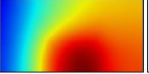
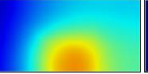

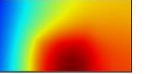

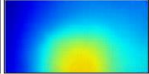
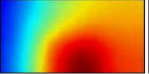
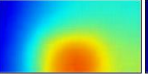

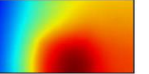
Original images						
Predicted value						

Table 4. Training results of the CA for the baseplate.

* For NNs, labels denote the real response values of evaluation of samples.

Original images						
Predicted value						

Subsequently, the compressed images are employed to train the WGAN. After training, the new $16 \times 16 \times 1$ gray level images generated by the generator of the WGAN are reshaped to their original distributions according the decoder of the CA, which are the purpose of the CWGAN. However, for generative models (e.g. GAN), it is difficult to evaluate their performance. Therefore, a recently proposed numerical assessment approach "Inception Score" [42] for quantitative evaluation is employed.

$$I = \exp\left(\mathbb{E}_{\mathbf{x}} D_{KL}(p(y|\mathbf{x}) \| p(y))\right) \quad (25)$$

Expand the exponent, then

$$I = \int_{\mathbf{x}} p(y|\mathbf{x}) \left[\log p(y|\mathbf{x}) - \log \int_{\mathbf{x}} p(y|\mathbf{x}) dx \right] dx \quad (26)$$

Nevertheless, infinitesimal calculus cannot be calculated. Therefore, the infinitesimal calculus is solved by using inverse summation operation.

$$I = \frac{1}{N} \sum_i^N p(y|x_i) \left[\log p(y|x_i) - \log \sum_j^N p(y|x_j) \right] \quad (27)$$

where \mathbf{x} denotes sample set; $p(y|\mathbf{x})$ is the softmax output of a trained classifier of the labels; and $p(y)$ is the overall labels distribution of generated samples.

The intuition behind this criterion is that a good model should generate diverse but meaningful images. Therefore, the KL divergence between the marginal distribution $p(y)$ and the conditional distribution $p(y|\mathbf{x})$ might be large. However, the score is not calculated directly for all generated images, but instead the generated images are broken up into chunks of size (N/n_{splits}) and the estimator is applied repeatedly on these chunks to compute a mean and standard deviation of the Inception Score. Generally, $n_{\text{splits}}=10$. The Inception Scores of the plate fins and baseplate are shown in Table 5.

Table 5. Inception Scores of the trained CWGAN.

Plate fins	Baseplate
------------	-----------

Mean score	2.805	2.367
Standard deviation	2.809e-05	1.009e-05

It can be seen that Inception Scores of the CWGAN are not very large. Considering that with the process of iteration and converge, the changes between different contour images are slightly. Accordingly, these Inception Scores might be satisfied and reasonable. Generated results are shown in Fig. 9, although some generated images lack convincing details and suffer blurred region, more than 95% results obtain the characteristics of contour images and generated images are useful and significant for contour image dataset. Importantly, CWGAN achieves satisfied results not by original but by compressed samples. Characteristics of compressed data are well achieved. It can be inferred that the performance of the CWGAN can be improved through dimensionality reduction.

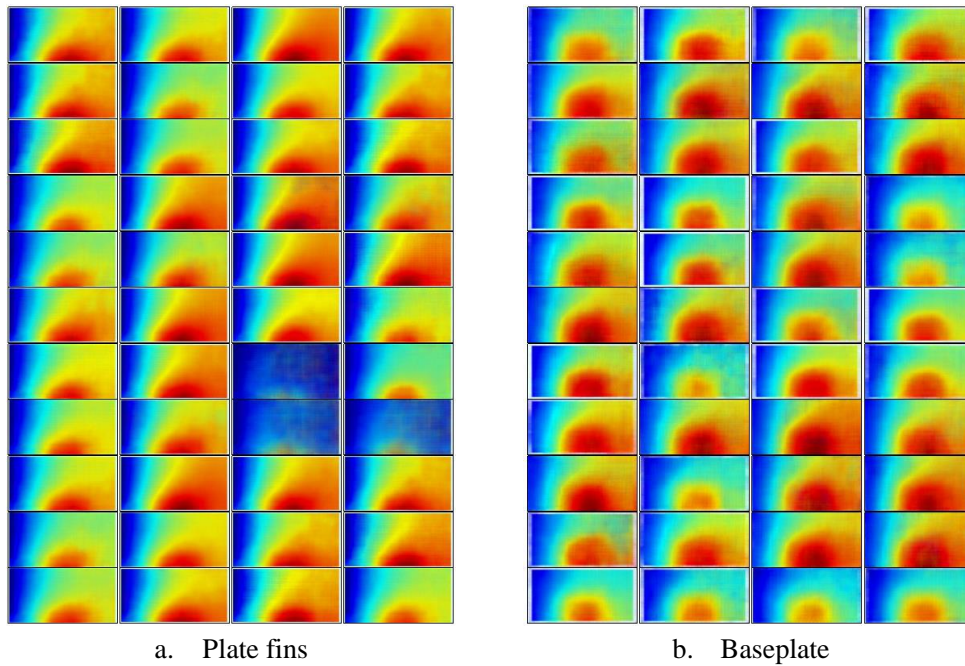


Fig. 9. Generated results by applying CWGAN.

4.4. Reconstruction of the heat transfer process

Each objective function (the highest temperature) of the generated image in Section 4.2 is calculated by trained CIC in Section 4.1. Then the Lagrange interpolation algorithm expressed by Eqs. (28) - (29) is used to complete the reconstruction task.

$$f(x) = \sum_{i=1}^n y_i p_i(x), i = 1, 2, \dots, n \quad (28)$$

s.t.

$$p_i = \prod_{j=1, j \neq i}^n \frac{x - x_j}{x_i - x_j} = \frac{(x - x_1)(x - x_2) \dots (x - x_n)}{(x_j - x_1) \dots (x_j - x_{j-1})(x_j - x_{j+1}) \dots (x_j - x_n)} \quad (29)$$

Considering the heat source is in the baseplate, therefore, the basis of reconstruction is the highest temperature of the baseplate. Finally, the reconstructed 3D heat transfer process is shown in Fig. 10. The images pointed in red are the original process, and the total iterations are 1,211. The images pointed in blue are the generated contour images by CWGAN, and the iteration number of reconstruction is extended to 5,000. Obviously, compared with the original output, about 4000 new samples are generated by the suggested method.

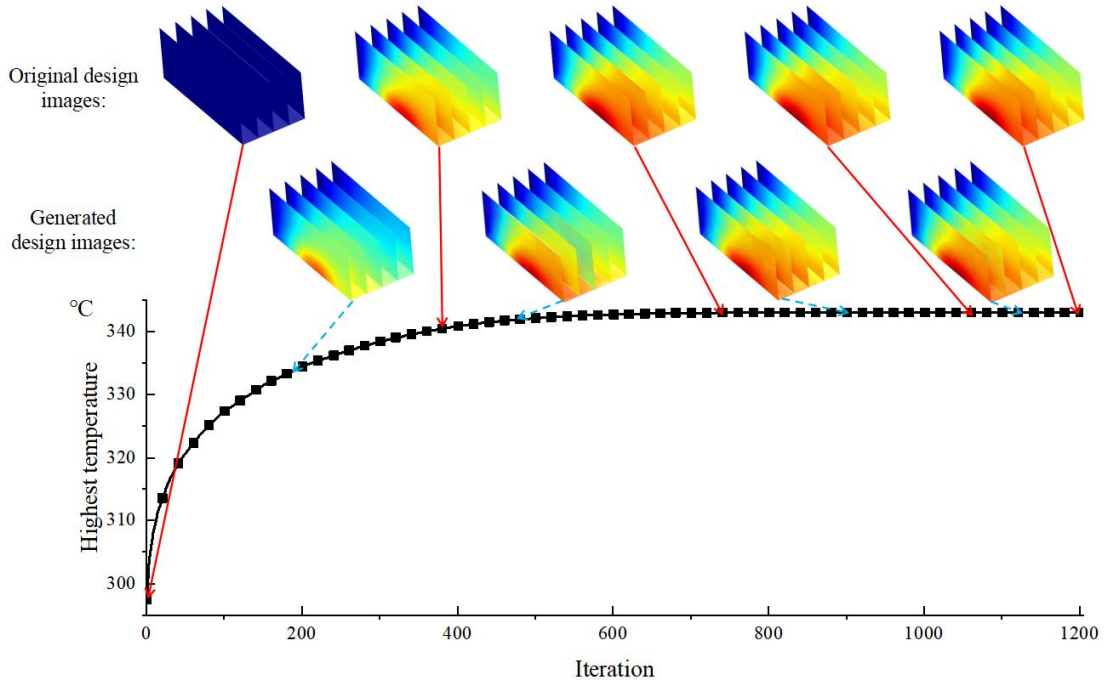


Fig. 10. The reconstruction of the heat transfer process of the PFHS.

In order to evaluate the reconstructed results, the generated results by the suggested method are compared with the simulation results directly with 5,000 iterations as shown in Fig. 11. It can be found the results are well matched, and the maximum Relative Error (RE) of the interpolation is 1.728E-2 which is small and

satisfied enough. It suggests that more useful data can be applied to modeling in fewer iterations and the accuracy of model based on the new images should be more accurate than the original one.

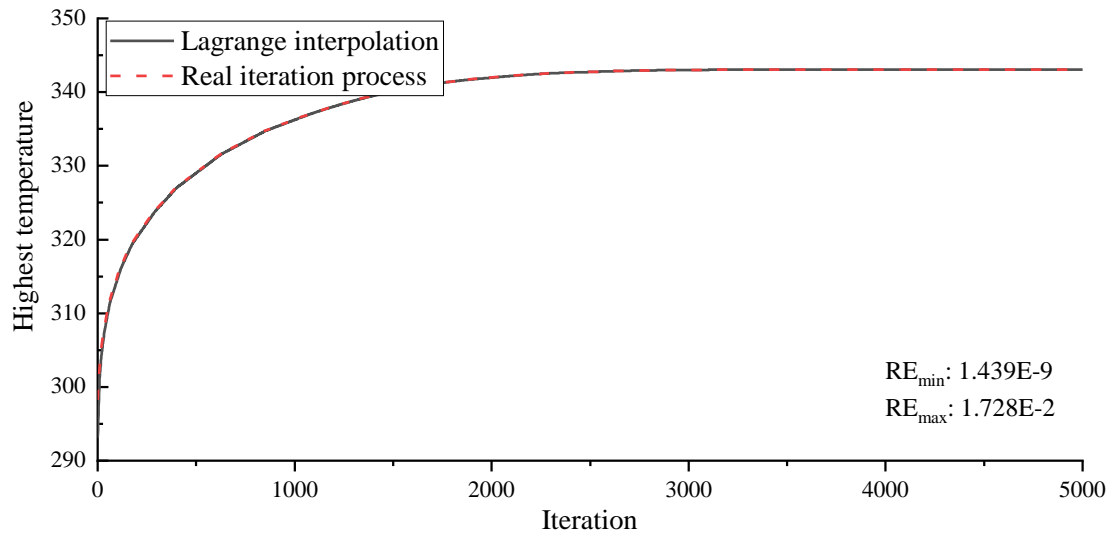


Fig. 11. Evaluation for the reconstructed results.

Conclusions

In this study, the ReConNN model is suggested for reconstruction of heat transfer processes, which can be further applied to researches such as modeling for time serial problems or some experiments which use high-speed photography to catch some dynamic characteristics and reconstruct the model through these photos. The main contributions of this study can be summarized as follows.

- i. The reconstruction method is implemented from image-based model to analysis-based model.
- ii. In order to finish the reconstruction task, a feasibility and efficient ReConNN model is suggested, which is integrated supervised learning and unsupervised learning algorithms.
- iii. A novel reconstruction method, 3D-2D-3D, for three-dimensional models is introduced. Namely the 3D model is cut into several slices according to its characteristics firstly, and then reconstruction is processed for each slice. Finally, all reconstructed slices are regrouped to a three-dimensional model.
- iv. According to a heat transfer process for a three-dimensional PFHS, the

reconstruction model shows a potential capability to reconstruct models for the simulation-based optimization problems.

Acknowledgments

This work has been supported by Project of the Key Program of National Natural Science Foundation of China under the Grant Numbers 11572120 and 51621004.

Reference

- [1]. Wang C-C, Lo J, Lin Y-T, Wei C-S. Flow visualization of annular and delta winglet vortex generators in fin-and-tube heat exchanger application. *International Journal of Heat and Mass Transfer*. 2002;45(18):3803-15.
- [2]. Ahmed H, Mohammed H, Yusoff M. An overview on heat transfer augmentation using vortex generators and nanofluids: approaches and applications. *Renewable and Sustainable Energy Reviews*. 2012;16(8):5951-93.
- [3]. Huisseune H, T'Joel C, De Jaeger P, Ameel B, De Schampheleire S, De Paepe M. Performance enhancement of a louvered fin heat exchanger by using delta winglet vortex generators. *International Journal of Heat and Mass Transfer*. 2013;56(1-2):475-87.
- [4]. Huisseune H, T'Joel C, De Jaeger P, Ameel B, De Schampheleire S, De Paepe M. Influence of the louver and delta winglet geometry on the thermal hydraulic performance of a compound heat exchanger. *International Journal of Heat and Mass Transfer*. 2013;57(1):58-72.
- [5]. Sinha A, Raman KA, Chattopadhyay H, Biswas G. Effects of different orientations of winglet arrays on the performance of plate-fin heat exchangers. *International Journal of Heat and Mass Transfer*. 2013;57(1):202-14.
- [6]. Chiang K-T. Optimization of the design parameters of Parallel-Plain Fin heat sink module cooling phenomenon based on the Taguchi method. *International communications in heat and mass transfer*. 2005;32(9):1193-201.
- [7]. Chingulpitak S, Wongwises S. A review of the effect of flow directions and behaviors on the thermal performance of conventional heat sinks. *International Journal of Heat and Mass Transfer*. 2015;81:10-8.
- [8]. Chen H-L, Wang C-C. Analytical analysis and experimental verification of interleaved parallelogram heat sink. *Applied Thermal Engineering*. 2017;112:739-49.
- [9]. Chen H-L, Wang C-C. Analysis and experimental verification of weight saving with trapezoidal base heat sink. *Applied Thermal Engineering*. 2018;132:275-82.
- [10]. Al-Damook A, Kapur N, Summers J, Thompson H. An experimental and computational investigation of thermal air flows through perforated pin heat sinks. *Applied thermal engineering*. 2015;89:365-76.
- [11]. Zhou F, Catton I. Numerical evaluation of flow and heat transfer in plate-pin fin heat sinks with various pin cross-sections. *Numerical Heat Transfer, Part A: Applications*. 2011;60(2):107-28.
- [12]. Joo Y, Kim SJ. Comparison of thermal performance between plate-fin and pin-fin heat sinks in natural convection. *International Journal of Heat and Mass Transfer*. 2015;83:345-56.

- [13]. Ventola L, Curcuruto G, Fasano M, Fotia S, Pugliese V, Chiavazzo E, et al. Unshrouded Plate Fin Heat Sinks for Electronics Cooling: Validation of a Comprehensive Thermal Model and Cost Optimization in Semi-Active Configuration. *Energies*. 2016;9(8):608.
- [14]. Hossain R, Culham JR, Yovanovich MM, editors. Influence of bypass on flow through plate fin heat sinks. *Semiconductor Thermal Measurement and Management Symposium, 2007 SEMI-THERM 2007 Twenty Third Annual IEEE*; 2007: IEEE.
- [15]. Li H-Y, Chao S-M. Measurement of performance of plate-fin heat sinks with cross flow cooling. *International Journal of Heat and Mass Transfer*. 2009;52(13-14):2949-55.
- [16]. Li H-Y, Chen C-L, Chao S-M, Liang G-F. Enhancing heat transfer in a plate-fin heat sink using delta winglet vortex generators. *International Journal of Heat and Mass Transfer*. 2013;67:666-77.
- [17]. Srisomporn S, Bureerat S. Geometrical design of plate-fin heat sinks using hybridization of MOEA and RSM. *IEEE Transactions on components and packaging technologies*. 2008;31(2):351-60.
- [18]. Jian-hui Z, Chun-xin Y, Li-na Z. Minimizing the entropy generation rate of the plate-finned heat sinks using computational fluid dynamics and combined optimization. *Applied Thermal Engineering*. 2009;29(8-9):1872-9.
- [19]. Rao R, Waghmare G. Multi-objective design optimization of a plate-fin heat sink using a teaching-learning-based optimization algorithm. *Applied Thermal Engineering*. 2015;76:521-9.
- [20]. Chen C-T, Chen H-I. Multi-objective optimization design of plate-fin heat sinks using a direction-based genetic algorithm. *Journal of the Taiwan Institute of chemical Engineers*. 2013;44(2):257-65.
- [21]. Chen H-T, Lai S-T, Haung L-Y. Investigation of heat transfer characteristics in plate-fin heat sink. *Applied Thermal Engineering*. 2013;50(1):352-60.
- [22]. Kim D-K. Thermal optimization of plate-fin heat sinks with fins of variable thickness under natural convection. *International Journal of heat and mass transfer*. 2012;55(4):752-61.
- [23]. Li Y, Wang H, Mo K, Zeng T. Reconstruction of Simulation-Based Physical Field with Limited Samples by ReConNN. *arXiv preprint arXiv:180500528*. 2018.
- [24]. Shiguemori ÉH, Da Silva JDS, de Campos Velho HF. Estimation of initial condition in heat conduction by neural network. *Inverse Problems in Science and Engineering*. 2004;12(3):317-28.
- [25]. Sablani S, Kacimov A, Perret J, Mujumdar A, Campo A. Non-iterative estimation of heat transfer coefficients using artificial neural network models. *International Journal of Heat and Mass Transfer*. 2005;48(3-4):665-79.
- [26]. Baby R, Balaji C. Experimental investigations on phase change material based finned heat sinks for electronic equipment cooling. *International Journal of Heat and Mass Transfer*. 2012;55(5-6):1642-9.
- [27]. Cz ę B, Woodbury KA, Gr óf G. Inverse identification of temperature-dependent volumetric heat capacity by neural networks. *International Journal of Thermophysics*. 2013;34(2):284-305.
- [28]. Razavi M, Dehghani-Sanij A, Khani M, Dehghani M. Comparing meshless local Petrov–Galerkin and artificial neural networks methods for modeling heat transfer in cisterns. *Renewable and Sustainable Energy Reviews*. 2015;43:521-9.
- [29]. Aminian A. Predicting the effective thermal conductivity of nanofluids for intensification of heat transfer using artificial neural network. *Powder Technology*. 2016;301:288-309.
- [30]. Colorado D, Ali M, Garc ía-Valladares O, Hernández J. Heat transfer using a correlation by neural network for natural convection from vertical helical coil in oil and glycerol/water solution. *Energy*. 2011;36(2):854-63.

- [31].Léon Y, Bottou L, Bengio Y, Haffner P. Gradient-based learning applied to document recognition. Proceedings of the IEEE. 1998;86(11):2278-324.
- [32]. Goodfellow I, Pouget-Abadie J, Mirza M, Xu B, Warde-Farley D, Ozair S, et al., editors. Generative adversarial nets. Advances in neural information processing systems; 2014.
- [33]. Lecun Y, Bottou L, Bengio Y, Haffner P, editors. Gradient-Based Learning Applied to Document Recognition. IEEE; 1998.
- [34]. Krizhevsky A, Sutskever I, Hinton GE, editors. ImageNet classification with deep convolutional neural networks. International Conference on Neural Information Processing Systems; 2012.
- [35]. Simonyan K, Zisserman A. Very Deep Convolutional Networks for Large-Scale Image Recognition. Computer Science. 2014.
- [36]. Radford A, Metz L, Chintala S. Unsupervised Representation Learning with Deep Convolutional Generative Adversarial Networks. Computer Science. 2015.
- [37]. Martin Arjovsky SC, Leon Bottou. Wasserstein Generative Adversarial Networks. Proceedings of the 34 th International Conference on Machine Learning, Sydney, Australia. 2017.
- [38]. Gulrajani I, Ahmed F, Arjovsky M, Dumoulin V, Courville A. Improved Training of Wasserstein GANs. 2017.
- [39]. Tong ABMVRSKBX. Sparse Autoencoder. CS294A Lecture Notes. 2011;vol. 72:1-19.
- [40]. Ioffe S, Szegedy C. Batch normalization: Accelerating deep network training by reducing internal covariate shift. arXiv preprint arXiv:150203167. 2015.
- [41]. Li Y WH. Can CNNs Construct Highly Accurate Model Efficiently with Limited Training Samples? [J]; arXiv preprint arXiv:1712.01639, 2017.
- [42]. Barratt S, Sharma R. A Note on the Inception Score. arXiv preprint arXiv:180101973. 2018.